EES Solar

PAPER

View Article Online
View Journal | View Issue

Cite this: *EES Sol.*, 2025, **1**, 1102

Sub-micron $Cu(In,Ga)Se_2$ solar cells with an efficiency of 18.2% enabled by a hole transport layer

Taowen Wang, *[a] Longfei Song,[b] Saeed Bayat,[a] Michele Melchiorre,[a] Nathalie Valle,[b] Adrian-Marie Philippe,[b] Emmanuel Defay,[b] Sebastjan Glinsek[b] and Susanne Siebentritt *[a]

Reducing the thickness of $Cu(In,Ga)Se_2$ solar cells is a key objective to reduce production cost and to improve sustainability. The major challenge for sub-micron $Cu(In,Ga)Se_2$ cells is the recombination at the backside. In standard $Cu(In,Ga)Se_2$ backside recombination is suppressed by a bandgap gradient, acting as a back surface field. This gradient is difficult to maintain in sub-micron absorbers. In this study, a hole transport layer passivates the back contact and enables efficient sub-micron $Cu(In,Ga)Se_2$ solar cells without the need for a Ga gradient. The backside passivation by the hole transport layer is as effective as an optimized Ga gradient, resulting in a significant increase in open-circuit voltage by 80 mV in comparison to the reference sample. Moreover, the hole transport layer exhibits good transport properties, leading to a fill factor as high as 77%. A photoluminescence quantum yield of 0.15% and efficiency above 18% are demonstrated in sub-micron $Cu(In,Ga)Se_2$ absorbers.

Received 3rd April 2025
Accepted 3rd October 2025

DOI: 10.1039/d5el00049a

rsc.li/EESSolar

Broader context

In recent years, the CIGSe solar cell community has sought a paradigm shift, aiming to transform the Ga gradient inhomogeneous absorber into a homogeneous one using a hole-selective transport layer (HTL). This alteration is anticipated to enhance efficiency while also presenting an opportunity for backside passivation in high bandgap, ultra-thin, and bifacial chalcopyrite solar cells. However, implementing the HTL in CIGSe solar cells poses a challenge due to the harsh growth conditions, such as high substrate temperature and a Se atmosphere, which typically result in the destruction of the HTL beneath the CIGSe layer due to inter-diffusion or selenization. This work represents a significant milestone for HTL application in CIGS solar cells and similar solar cells grown under harsh conditions, requiring the stability of buffer layers. With this breakthrough work, we successfully achieved a record efficiency of 18.2% for ultra-thin (750 nm) CIGS solar cells.

Introduction

$Cu(In,Ga)Se_2$ (CIGS) based thin film solar cells represent one of the photovoltaic (PV) technologies with the highest efficiencies of 23.6% and proven stability.[1–4] However, these record CIGS solar cells are typically achieved using a rather thick absorber layer of ~2 μm thickness. While this thickness allows for high efficiency, it also demands a larger quantity of raw metals, such as In and Ga, resulting in higher production and environmental cost. Reducing the thickness of the absorber layer presents a compelling opportunity to decrease material consumption. However, the efficiency of these solar cells cannot be compromised since the cost of electricity generation is directly influenced by the efficiency. Higher efficiency translates to lower system costs, making it a key factor in driving cost-effectiveness of PV electricity.

Reducing the absorber thickness leads to challenges for the open circuit voltage, as well as for the short circuit current. The reduction in short circuit current is mainly due to reduced absorption in thinner layers. Experiments and simulations show that the absorption loss becomes severe only for absorbers of 500 nm and below.[5] Absorbers that thin require advanced light management techniques.[6–9] However, in the range from 500 to 1000 nm absorber thickness, the efficiency is reduced mostly because of a significant decrease in open-circuit voltage V_{oc} due to backside recombination.[10,11] The back contact interface between the molybdenum layer and the CIGS absorber exhibits a high recombination velocity exceeding 10^5 cm s^{-1}.[12–14] When the absorber layer is thinner, photogenerated carriers can more easily reach the back contact. This increases the non-radiative recombination at the back interface, which in turn reduces the photoluminescence quantum yield (PLQY). The lower PLQY directly contributes to a reduced open-circuit

[a]*Laboratory for Photovoltaics (LPV), Department of Physics and Materials Science, University of Luxembourg, 41 rue du Brill, L-4422, Belvaux, Luxembourg. E-mail: wangtaowenscu@hotmail.com; susanne.siebentritt@uni.lu*

[b]*Luxembourg Institute of Science and Technology (LIST), 41 rue du Brill, L-4422, Belvaux, Luxembourg*

voltage (V_{oc}) and overall degradation in solar cell performance. To address backside recombination in standard CIGS solar cells, a Ga gradient is employed, introducing a conduction band increase towards the backside, which drives minority carriers away from the back contact, thereby reducing backside recombination, similar to a back surface field. Simulations have shown that the efficiency of sub-micron CIGS solar cells can be above 20% with a well passivated back surface.[15] In our previous study,[16] we showed by experiments and simulations a significant improvement in V_{oc} by reducing backside recombination for $CuInSe_2$ solar cells with a Ga backside gradient even in thick absorbers. However, when dealing with thinner absorbers, the limited deposition duration and reduced thickness of the absorber pose challenges in establishing the necessary Ga gradient. To mitigate backside recombination experimentally, extensive experimentation has demonstrated the necessity of a dedicated and intricate 3-stage process to grow a CIGS absorber with a sufficiently steep conduction band gradient towards the back contact.[17–20] By optimizing the Ga gradient, the best efficiency, so far, of 17.5% has been achieved using 900 nm CIGS with an anti-reflection coating.[19] However, there are some issues with the required steep Ga gradient towards the backside of sub-micron CIGS solar cells. Firstly, the exact shape of the Ga gradient has a significant impact on the performance of solar cells,[21] necessitating highly reproducible processes with minimal tolerance for fluctuations. This requirement may hinder large-scale production. Secondly, the region with a high Ga/(Ga + In) ratio has been observed to exhibit a high recombination rate, resulting in a low minority carrier lifetime of approximately 100 ps,[22] in line with the observation of deep defects for Ga/(Ga + In) ratios >0.5.[23] Moreover, the bandgap gradient limits the effective absorption of low-energy photons due to the reduced thickness of the band gap minimum region.[24] Consequently, this leads to higher losses of low-energy photons in J_{sc}. In addition, the necessary steep bandgap gradient results in higher radiative V_{oc} losses.[25–27]

To overcome these challenges, implementing a hole selective transport layer (HTL) is an effective solution. The HTL should exhibit high resistance to minority carriers (electrons) and low resistance to majority carriers (holes). This function can be achieved through, for example, asymmetric conductivity and band offsets.[28,29] By employing this configuration, the minority carrier density dependent surface recombination can be minimized, and majority carriers can be freely transported. The concept of utilizing a HTL as a replacement for the Ga gradient holds significant promise. However, identifying a suitable material that can withstand the harsh growth conditions of CIGS, such as high temperature and selenium (Se) pressure, has been a challenge.

Recently,[30] we successfully developed a functional HTL with good backside passivation and efficient hole transport properties. This HTL is prepared as a $CuGaSe_2$ layer covered by solution combustion synthesis prepared In_2O_3, which during the absorber growth process converts into $CuInSe_2/GaO_x$. Solution combustion synthesis is practical for laboratory-scale or wafer type production. However, since it involves spin coating that cannot be scaled to the m^2 sized substrates of the thin film PV industry. Therefore, we additionally explore sputtered In_2O_3 in this study. We demonstrate that sputtered In_2O_3 matches the performance of solution processed In_2O_3 in terms of passivation and hole transportation, resulting in similarly improved V_{oc} and fill factor (FF), showing promising prospects for large-scale application of this novel hole transport layer. Applying this HTL to sub-micron $Cu(In,Ga)Se_2$ enhances V_{oc} by up to 80 mV while maintaining a FF of 77%. Further enhancement through rubidium fluoride (RbF) post-deposition treatment (PDT) yields a good photoluminescence (PL) quantum yield (Y_{PL}) of 0.15% and an efficiency of 18.2% (active area) for sub-micron CIGS solar cells covered by an anti-reflection coating (ARC). An efficiency of 16.2% (full-area) has been certified. The difference can be attributed to non-optimised contact grid area, which blocks lights and results in loss of J_{sc}.

Studied samples

The samples analyzed in this study are briefly introduced here, with detailed sample preparation procedures discussed in the Methods section. The general sample structure is glass-Mo-(HTL-)CIGS-CdS-ZnO-ZnO:Al-Ni/Al grids(MgF_2), as shown in Fig. 6a. Reference samples, denoted as MoRe, consist of CIGS directly grown on Mo without a HTL. The HTL is grown as a $CuGaSe_2/In_2O_3$ stack deposited on Mo prior to absorber deposition. This stack transforms into $Cu(In,Ga)Se_2/GaO_x$ during absorber deposition, as elaborated below. The thickness of the original $CuGaSe_2$ layer ranges from around 100 nm to 200 nm, while In_2O_3 thickness varies from 10 nm to 40 nm. The $CuGaSe_2$ layer is prepared *via* co-evaporation at a substrate setting temperature of 356 °C, with a Cu/Ga ratio of 0.9–0.95 determined by energy-dispersive X-ray spectroscopy (EDS). In_2O_3 deposition is achieved through either solution combustion synthesis or RF sputtering. Prior to absorber deposition, this stack ($Glass/Mo/CGS/In_2O_3$) undergoes annealing at a substrate setting temperature of 500 °C for 20 minutes under vacuum of $\sim 5 \times 10^{-9}$ torr, with or without a ~40 nm layer of Cu on top. Cu annealing enhances hole transport through the HTL, as discussed later. Although we believe that the CIGS part of the HTL cannot contribute to J_{sc} because the photo-generated electrons cannot pass through the GaO_x due to the high conduction band offset, we address the concern about the actual absorber thickness, by adding the thickness of CIGS in the HTL to the actual absorber thickness. The total thickness is written as "thickness of CIGS in the HTL + CIGS absorber thickness". The thickness of absorbers is determined by using the cross-sectional SEM image as shown in Fig. S1. The CIGS absorber for the record sub-micron (0.10 + 0.75) μm solar cells with an active area efficiency of 18.2% is prepared using a 3-stage process,[31,32] with the 1st stage substrate setting temperature at 500 °C and 580 °C for the 2nd and 3rd stages. For all other CIGS absorbers, the 1st stage substrate temperature is 356 °C, with subsequent stages at 580 °C. The higher temperature in the 1st stage aims to enhance grain size and improve absorber quality. RbF PDT, if applied, is carried out immediately after the absorber growth without vacuum interruption. It's done at a substrate setting temperature of 280 °C under a Se

flux of ~2.5 × 10^{-6} torr for 10 minutes, with an RbF source temperature of 450 °C. All discussed samples are coated with chemical bath deposited CdS, approximately 50 nm thick. Prior to CdS deposition, samples undergo etching in 5% KCN aqueous solution for 30 s; RbF-treated samples are additionally etched in 1.5 M NH_4OH for 3 minutes after KCN etching. To complete solar cell devices, an intrinsic zinc oxide/aluminum-doped zinc oxide stack is RF sputtered as a window layer, and a grid of Ni/Al is evaporated as a front contact. The record solar cell is covered with 90 nm MgF_2 as an ARC. Some samples are treated by heat light soaking: absorbers covered with the CdS buffer undergo treatment in a N_2 atmosphere at a substrate setting temperature of 80 °C, with an equivalent illumination intensity of 0.5 Sun and a duration of 3 hours.

Ion exchange between In and Ga in the HTL

In a previous study,[30] the functionality of this HTL has been demonstrated for $CuInSe_2$ solar cells without Ga in the absorber with a bandgap of around 1.0 eV. The HTL exhibits thermal stability, remaining physically at the backside despite the harsh growth conditions of the absorber. On the other hand, complete ion exchange between In and Ga occurs, converting $CuGaSe_2/In_2O_3$ into $CuInSe_2/GaO_x$. In the present study, we reaffirm the thermal stability of the HTL and the ion exchange process in the presence of Ga containing absorbers with a somewhat wider band gap. We analyse a sample in detail after the absorber process, which is made from a solution deposited In_2O_3 layer with Cu annealing. Cross-section images from scanning transmission electron microscopy in Fig. 1a clearly depict the individual layers between the Mo back contact and the absorber. These layers are further distinguishable through EDS mapping of the same area. The top part of the back contact is identified as $MoSe_2$, rich in Mo and Se as shown in Fig. 1b and c, consistent with previous reports.[33,34] The subsequent layer is identified as $Cu(In,Ga)Se_2$, as Cu, In, Ga, and Se are detected (Fig. 1c–f). Additionally, a 30–40 nm thick layer is observed to be rich in O and Ga, with minimal In and Se content, strongly suggesting an exchange of In and Ga, leading to GaO_x formation from the original In_2O_3, as observed in prior work.[30] However, unlike the case of pure CIS absorbers, where the CGS beneath the oxide layer completely converts into CIS after absorber deposition,[30] in the case of CIGS absorbers, Ga is still present beneath the oxide layer. The Ga concentration, measured as the Ga/(Ga + In) ratio, is comparable to that of the absorber layer above the oxide layer, as can be seen from the Ga and In profiles in Fig. 1h. Diffusion is primarily driven by temperature and concentration differences, and the process appears to reach equilibrium when the Ga contents on both sides of the oxide are equal. Nonetheless, whether the bottom layer of the HTL is $CuInSe_2$ or $Cu(In,Ga)Se_2$, no discernible differences in passivation are

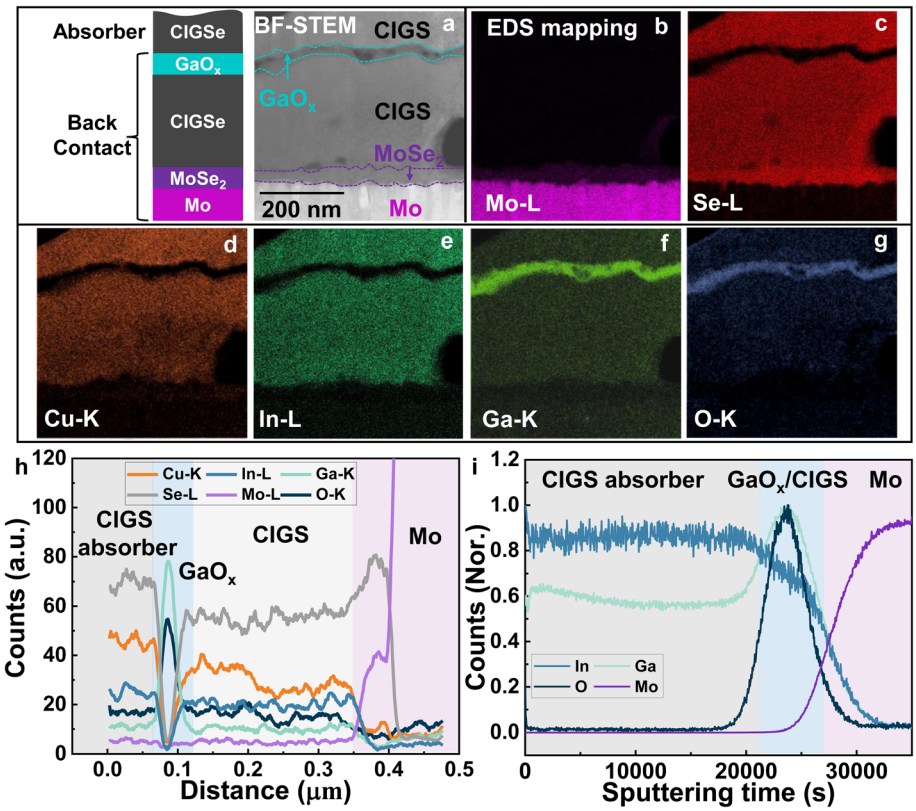

Fig. 1 (a) Bright field (BF) scanning transmission electron micrograph (STEM). From bottom to top, the back contact region consists of Mo, $MoSe_2$, CIGS and GaO_x, in which the CIGS and GaO_x are formed from $CuGaSe_2/In_2O_3$ *via* ion exchange between Ga and In; the EDS mapping of the same as the scanning transmission electron micrograph: (b) Mo; (c) Se; (d) Cu; (e) In; (f) Ga; (g) O. (h) EDS line scans across the back contact interfaces. (i) SIMS depth profiles show that there is no Ga gradient in the absorber towards the backside.

observed, as demonstrated by the performance of the ensuing solar cells, discussed below.

Furthermore, the same Ga content between the CIGS layers on both sides of the GaO_x could also indicate that there is no Ga gradient toward the backside of the samples. However, the absorber thickness studied in TEM-EDS mapping (Fig. 1e and f) or line scans (Fig. 1h) is insufficient to confirm the absence of a Ga gradient over the whole depth of the absorber. To address this concern, secondary ion mass spectrometry (SIMS) is conducted on the same sample as the one studied by TEM. As the system is not calibrated for CIGS (since no standard sample has been available), the non-absolute SIMS data are presented in Fig. 1i, where each element distribution is normalized to its maximum within the measured range. Although the depth resolution of the low-energy SIMS used is a few nanometers, it increases to a few tens of nanometers due to the roughness of the different interfaces in the stack. Thus, individual CIGS and GaO_x layers cannot be distinguished at the backside, but the interface between the absorber and GaO_x can be located where the oxygen signal is half of its maximum. The slight increase in Ga counts in this region is due to the presence of GaO_x in the sputtered material during SIMS analysis, which also corresponds to the observed increase in oxygen counts. The region marked in blue in Fig. 1i can be identified with the HTL containing GaO_x/CIGS (from left to right). The absorber is to the left of the blue region, and the Mo back contact is to the right. It is evident that the Ga and In compositions remain constant over most of the absorber depth, in particular towards the backside, indicating the absence of a Ga gradient that would passivate the back contact. Therefore, any observed passivation in our samples is solely attributed to the HTL rather than a Ga gradient. However, a small Ga gradient towards the front side persists. Although the front side Ga gradient may help mitigate front surface recombination,[35] it becomes unnecessary when adequate passivation is achieved through methods such as proper band alignment[36–38] and heavy alkali PDT.[1,38,39] Consequently, a completely homogeneous absorber would improve collection of long-wavelength photons and reduce radiative losses in V_{oc}.[25]

We attribute the flat Ga profile towards the backside to two main factors. Firstly, establishing a suitable Ga gradient within a constrained absorber thickness requires an optimized 3-stage process, where the Ga/In flux ratio during the 1st stage is significantly higher than that of the 3rd stage.[15] However, in our approach, we maintain the same Ga/In flux ratio in both the 1st and 3rd stages. Secondly, in the case of the Cu-annealed sample, absorber growth starts with Cu-rich CIGS rather than $(In,Ga)_2Se_3$ precursors. This variation influences the reaction rate of Ga and In compounds with Cu during the 2nd stage, ultimately resulting in a flat Ga distribution towards the backside. As has been demonstrated in the past, when Cu is present throughout the absorber process, the Ga profile becomes much flatter and is only controlled by the Ga/In flux ratios during the time of the process.[1,21,40]

Good passivation but hole transport blocking

The as-grown HTL consists of approximately 100 nm $CuGaSe_2$ covered by approximately 40 nm solution deposited In_2O_3. The layers after the absorber process are clearly visible in SEM cross-section images (see Fig. S1). To evaluate the passivating effect of the HTL for sub-micron CIGS, time resolved PL (TRPL) analysis is performed on two sub-micron CIGS films deposited on the HTL and directly on Mo, both grown in a classical 3-stage process without a Cu-annealing step at the beginning (Fig. 2a). The two absorbers are grown by the same co-evaporation process and the CdS front passivation layer is deposited by the same chemical bath process. The decay is best described as bi-exponential. The longer-term lifetime τ_2 obtained from the 2-exponential fitting is used in the following as minority carrier lifetime, as it is more sensitive to backside recombination and therefore provides a better indication of passivation effects.[41] As illustrated in Fig. 2a, the lifetime of the HTL passivated sample improved significantly from 19 to 161 ns compared to the reference without a HTL. Given that these samples are prepared by the same absorber and CdS processes, it is reasonable to infer that they have similar bulk and front surface lifetimes. Therefore, the longer τ_2 indicates effective backside passivation, meaning a reduction in backside recombination. Further evidence for the passivation is provided by absolute photoluminescence spectroscopy, which allows the extraction of the quasi-Fermi level splitting ΔE_F from a fit to Planck's generalised law and separately the non-radiative ΔE_F loss from the PL quantum yield Y_{PL} $[k_bT \times \ln(Y_{PL})]$[26,42,43] Fig. 2b and c show that the HTL increases ΔE_F by about 80 meV, the same amount by which the non-radiative loss is reduced. However, when investigating the ensuing solar cells (Fig. 2c and d) we detect two problems: the increase in V_{oc} is lower than the increase in ΔE_F and the FF is very poor. The difference between ΔE_F and V_{oc} indicates a gradient in at least one of the quasi Fermi levels, which occurs at or near the contacts.[44] We attribute this additional loss to hole transport blocking in the HTL, which restricts the forward diode current, resulting in a linear behavior of the J–V curve, as depicted in Fig. 2d. Consequently, this leads to an extremely low FF of approximately 30%, compared to the reference sample's FF of approximately 76%. This unfavorable blocking is primarily attributed to the high valence band offset between GaO_x and the absorber, as previously discussed.[30] We had also proposed that the hole transport properties of GaO_x are closely linked to the amount of Cu present. Cu can introduce deep defects in GaO_x near the valence band maximum of CIGS, assisting hole transport.[45,46] To address the issue of hole transport, here, we experiment with reducing the thickness of In_2O_3 and introducing an additional Cu annealing process to the oxide layer, aiming to enhance its hole transport properties.

Reducing the thickness of In_2O_3

Previous studies indicate that reducing the thickness of oxide layers, like Al_2O_3 (ref. 47–49) and TiO_2,[50,51] has demonstrated an improvement in hole transport, leading to an increased fill factor (FF), but usually with a trade-off in passivation and consequently reduced V_{oc}. This trade-off between the FF and V_{oc} generally hinders the achievement of high-efficiency solar cells. Consistent with these findings, our study also reveals a similar trade-off (see Fig. S2a and b). Decreasing the thickness of In_2O_3 from 40 nm to 20 nm and 10 nm progressively enhances the FF

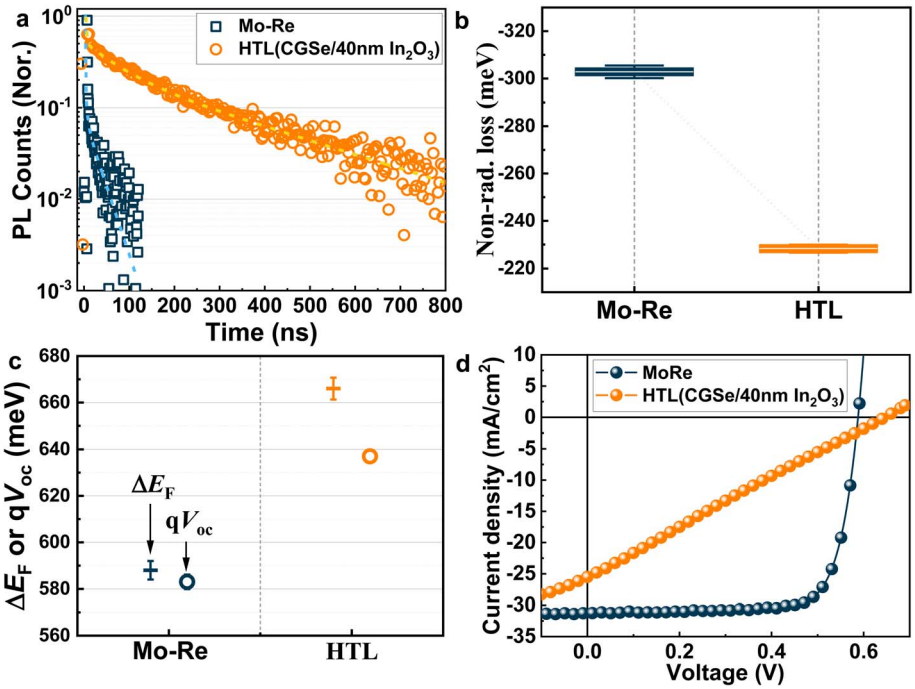

Fig. 2 (a) TRPL measurements of the reference sample and sample passivated by the HTL made from 40 nm solution processed In_2O_3. The good passivation of the HTL increases the lifetime of the sample from ~19 to 161 ns. (b) Non-radiative loss in ΔE_F of the two samples, which is determined by $k_bT \times \ln(Y_{PL})$. (c) Comparison of ΔE_F and qV_{oc} of these samples. Due to hole transport blocking caused by the HTL, the limited forward diode current results in an additional V_{oc} loss, $\Delta E_F - qV_{oc}$. (d) Current density *vs.* voltage characteristics under illumination, indicating an extremely low FF of the HTL passivated sample due to blocking of hole transport.

of the solar cells. Notably, solar cells with 10 nm In_2O_3 exhibit a nearly identical FF (~77%) compared to the reference sample, indicating successful removal of hole transport blocking. However, the non-radiative ΔE_F loss of samples with thinner In_2O_3 is 20–30 meV higher than that of samples with thicker In_2O_3, suggesting that excessively thin oxide layers fail to provide adequate backside passivation.

Cu annealing: making the HTL conductive for holes

To address the trade-off between passivation and hole transport, we introduce additional Cu annealing prior to the absorber deposition. This Cu annealing is considered because our previous work[30] has demonstrated that utilizing a Cu-rich $CuGaSe_2$ layer enables hole transport, suggesting that extra Cu may play a crucial role in hole transport. Furthermore, it has been observed that Cu can introduce deep defects in GaO_x, which may facilitate hole transport: this hole transport has been demonstrated in perovskite solar cells through GaO_x[45] or Ga_x-$In_{2-x}O_3$ (ref. 46) doped with Cu. In_2O_3, from which the GaO_x is formed during absorber deposition, is prepared either by solution combustion synthesis or by RF sputtering, with thicknesses of 20, 30, and 40 nm for solution deposited In_2O_3, and 30, 35, and 40 nm for sputtered In_2O_3. In all cases, approximately 40 nm of Cu is evaporated onto the surface of In_2O_3 at a substrate setting temperature of 200 °C. Subsequently, the temperature is rapidly increased from 200 to 500 °C at a rate of 50 °C per minute, followed by annealing under vacuum (~5×10^{-9} torr) at 500 °C for 20 minutes. Afterward, the substrate is cooled to 356 °C before the deposition of CIGS *via* a 3-stage process. The thickness of the absorbers deposited onto In_2O_3 prepared by solution combustion synthesis or RF sputtering is approximately (0.20 + 0.90) μm and (0.10 + 0.75) μm, respectively, determined through SEM cross-section imaging (see Fig. S1). We remind here that the actual absorber thickness is 0.90 or 0.75 μm; the first number in the sum gives the thickness of the Cu(In,Ga)Se_2 layer underneath the oxide layer. As indicated in the literature, a CIGS thickness of around 1 μm is barely sufficient to avoid J_{sc} loss due to non-absorption.[6–9,52–54] Hence, the (0.20 + 0.90) μm and (0.10 + 0.75) μm CIGS absorbers may exhibit some non-absorption loss of J_{sc}, as will be discussed further.

To evaluate the passivation of the Cu-annealed HTL, TRPL analysis is conducted (Fig. 3a). Both solution and sputter-prepared In_2O_3, each with a thickness of 30 nm and labeled as "SCS30" and "SP30" respectively, exhibit a notable enhancement in lifetime. Specifically, when compared to the reference sample, the lifetime τ_2 increased from 19 ns to 164 ns and 264 ns for the SCS30 and SP30 samples, respectively. The fast initial decay observed in the MoRe reference sample and the passivated SP30 sample can be due to many causes (surface recombination, potential fluctuations or drift in space charge regions formed at grain boundaries or at the surface). The substantial improvement in the lifetime τ_2 confirms the effectiveness of the passivation. Furthermore, as shown by the EQE spectra (Fig. 3b), the good backside passivation is demonstrated by the better collection of photogenerated carriers, especially for long-wavelength photons that penetrate deep into the absorber and reach the backside. As illustrated further below

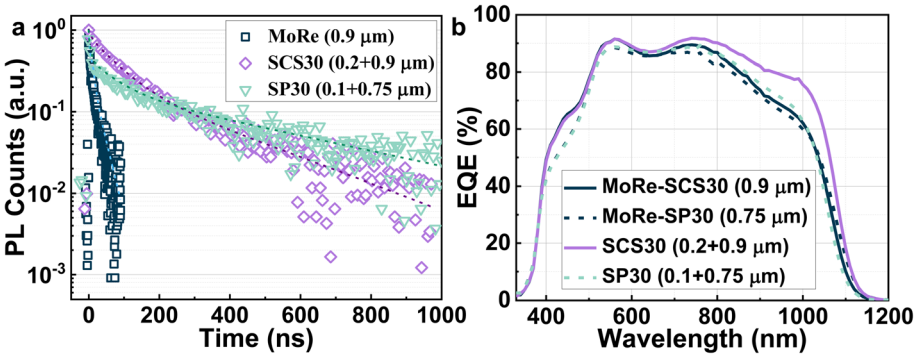

Fig. 3 (a) TRPL measurements of a reference sample without a HTL and samples passivated by a Cu-annealed HTL, prepared from a solution deposited or sputtered In_2O_3 layer with a thickness of 30 nm, labeled as SCS30 and SP30, respectively. With the HTL, the lifetime significantly increased from 19 ns to 164 ns and 264 ns for the SCS30 and SP30 samples, respectively, confirming the effective passivation achieved by either HTL. (b) The EQE spectra of solar cells passivated by the Cu-annealed HTL, together with their respective unpassivated references, demonstrate enhanced collection of long-wavelength photons, further supporting good backside passivation provided by the Cu-annealed HTL.

(Fig. 5d), this passivation increases the current density by 1.5 mA cm^{-2} for the solar cell with an absorber thickness of (0.2 + 0.9) μm (SCS30). For the solar cells with a thinner absorber of (0.10 + 0.75) μm (SP30 and the corresponding Mo–Re), the enhancement of the long-wavelength EQE is much less pronounced. This reduced effect of the passivation can be attributed to non-absorption losses, which reduce the effect of passivation on the EQE.

We investigate In_2O_3 layers of different thicknesses, all with Cu annealing, and obtain similar passivation effects to 30 nm In_2O_3, leading to nearly identical TRPL decay and EQE responses, as depicted in Fig. S3. The robustness of the HTL is encouraging, as it enables tolerance to thickness variations. Taking advantage of this, precise control of In_2O_3 thickness within a few nanometer ranges becomes unnecessary, which holds significant implications for large-scale manufacturing by enhancing reproducibility. Furthermore, it will be demonstrated later that the high FF is only minimally impacted by In_2O_3 thickness, when Cu-annealing is provided, underscoring its potential for large-scale application.

All samples are analysed by absolute PL. The effective passivation yields a notable enhancement in Y_{PL} of more than an order of magnitude, consequently reducing the non-radiative ΔE_F loss by 60–80 meV relative to the reference sample. As depicted in Fig. 4a by the square symbols, the non-radiative ΔE_F losses are derived from Y_{PL} according to $[k_bT \cdot \ln Y_{PL}]$. Both solution and sputter prepared HTLs exhibit considerably lower non-radiative ΔE_F loss than the reference sample on Mo, and the non-radiative losses come down to 220–240 meV. No correlation between In_2O_3 thickness and non-radiative ΔE_F loss is evident. This absence of a trend is likely attributable to differences in the absorber or front surface passivation at the interface with the CdS buffer. We often observe differences of 10 meV in ΔE_F for different samples, prepared under supposedly identical conditions. Thus, we conclude that the effect of backside passivation tends to saturate when the In_2O_3 thickness is 20 nm or more, where the backside recombination is reduced to a level that has little impact on ΔE_F of our samples with lifetimes in the range of 100 to 200 ns. However, the level of backside recombination could become more critical if the absorber's bulk lifetime is enhanced through other techniques, such as Ag alloying or heavy alkali PDT. Therefore, it appears safer to use HTLs based on In_2O_3 layers, somewhat thicker than the minimum thickness of 20 nm. Because of this, when investigating the effect of RbF PDT on our samples, all samples employ a 30 nm thickness of In_2O_3 to minimize the influence of backside recombination.

Besides the non-radiative loss from Y_{PL}, absolute PL allows the direct and independent determination of ΔE_F from a fit of the PL spectra to Planck's generalized law. The ΔE_F deficit is then defined as $(\Delta E_F^{SQ} - \Delta E_F)$, where ΔE_F^{SQ} represents the quasi Fermi-Level splitting of the Shockley–Queisser (SQ) limit. The bandgap used to determine ΔE_F^{SQ} is taken as the inflection point of the onset of the absorptance spectrum $[A(E)]$.[25] The absorptance spectrum is extracted from the PL spectrum, using Planck's generalised law, as explained in detail in the Methods section. As an example, Fig. 4b displays $A(E)$ and $dA(E)/dE$ of the sample with the best Y_{PL}. Due to the noise in $dA(E)/dE$, a Gaussian fit is applied to the noisy curve, as shown (after normalisation) by the orange dotted line. As shown by the normalised PL spectrum, its maximum is shifted to a lower energy than the band gap by about 25 meV, which is expected based on the gradual absorption edge.[26,55] The gradual absorptance increase can be attributed to a Ga gradient,[56,57] which is not the case here, and to tail states[56,58,59] and potential fluctuations.[60–63] The smoother the absorptance edge, the larger the radiative ΔE_F loss as well as the shift between the band gap and PL maximum.[26,61] The measured ΔE_F is reduced from the SQ limit by radiative and non-radiative losses. The complete loss is depicted in Fig. 4a by circles. All the points lie almost on the dashed blue line, which is 16 meV above the black line of the non-radiative loss. This difference indicates a constant value of the radiative loss of 16 meV in addition to the non-radiative loss. The radiative loss here is much lower than the reported value of 36 meV for traditional CIGS with a Ga gradient.[25] The low value of the radiative loss is attributed to the absence of a gradient (Fig. 1i). Optimizing the absorber to be fully homogeneous in depth and closer to stoichiometry may further

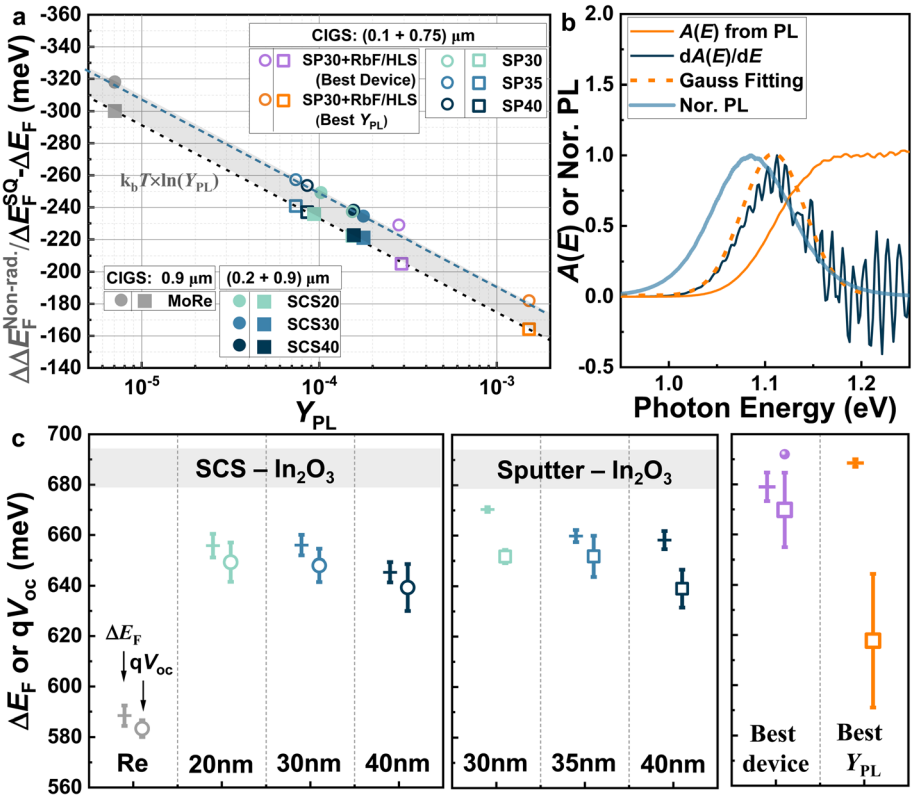

Fig. 4 (a) Non-radiative quasi-Fermi level splitting ΔE_F loss [$\Delta\Delta E_F^{Non\text{-}rad.} = k_bT \times \ln Y_{PL}$] (squares) and independently measured quasi-Fermi level splitting ΔE_F deficits with respect to the Shockley–Queisser (SQ) limit ($\Delta E_F^{SQ} - \Delta E_F$) (circles) as a function of Y_{PL}. Solid symbols: solution processed HTLs and the Mo reference; open symbols: sputter processed HTLs. The non-radiative loss is also described by the grey line. The dark dashed line is a fit to the ΔE_F loss and is about 16 meV higher than the non-radiative loss due to additional radiative loss. Additional samples with RbF post-deposition treatment and heat-light soaking (HLS) are given. (b) Absorptance spectrum $A(E)$, derivative of the absorptance spectrum $dA(E)/dE$ together with a Gaussian fit (normalised) and normalized PL spectrum of the sample with the best Y_{PL}. (c) ΔE_F and qV_{oc} for different solar cells. Both types of HTLs show a similar improvement in ΔE_F and qV_{oc} of ~70 meV in comparison to the reference solar cells. The somewhat lower qV_{oc} compared to the ΔE_F is most likely due to the front surface recombination. The high V_{oc} deficit of the sample with the best Y_{PL} is caused by the blocked diode current.

reduce the radiative ΔE_F loss by several meV. However, this improvement is relatively small when considering the non-radiative ΔE_F loss. Thus, the ΔE_F loss in CIGS is by far dominated by non-radiative loss, as was observed before.[30,64]

Quasi-Fermi level splitting gives us the potential V_{oc} of the finished solar cell; it is of course essential to measure V_{oc} in actual solar cells. Fig. 4c demonstrates improvement in V_{oc} for a HTL-passivated solar cell, very similar to the ΔE_F improvement. Both solution and sputter deposited In_2O_3 result in improved V_{oc} ranging between 640 and 660 mV, about 70 mV higher than the V_{oc} of the reference sample (~580 mV). This reaffirms that sputtered In_2O_3 is a viable alternative to solution prepared In_2O_3, thus paving the way for potential large-scale manufacturing applications. While the qV_{oc} of solar cells with sputter In_2O_3 is marginally lower than their corresponding ΔE_F, this discrepancy is likely attributed to front surface recombination, which tends to lower the quasi-Fermi level of electrons toward the front contact.[44] From numerous Cu(In,Ga)Se_2 solar cells, prepared in different labs and measured by our lab, we find in reasonably good devices a difference between V_{oc} and ΔE_F that varies from 5 to 20 meV,[44,65] potentially stemming from systemic deviations in device preparation. However, this variation does not affect the conclusion that HTL passivation substantially enhances V_{oc} compared to reference solar cells.

Achieving high-efficiency solar cells relies on achieving both effective passivation (yielding high V_{oc}) and efficient hole transport (resulting in a high FF). The J–V curves of the reference solar cell and those passivated by the Cu-annealed HTL, employing either 30 nm solution or sputter prepared In_2O_3, are presented in Fig. 5a. The diode character of the J–V characteristics indicates a comparable FF to the reference cell, coupled with a noticeable increase in V_{oc}. V_{oc} and FF distributions are summarized in Fig. 5b and c, respectively. The passivated samples exhibit a V_{oc} enhancement of 70 mV and good FF ranging from 70% to 76%. As a result, the efficiency is elevated from ~14% to over 16% for solar cells with solution prepared In_2O_3. Solar cells with sputtered In_2O_3 demonstrate a slightly lower efficiency of ~15.5% due a lower current, which might be attributed to the thinner absorber (0.1 + 0.75 µm), leading to J_{sc} losses due to non-absorption, as illustrated in Fig. 5d and 3b. These outcomes underscore the effectiveness of Cu annealing in improving hole transport properties through the final GaO_x film

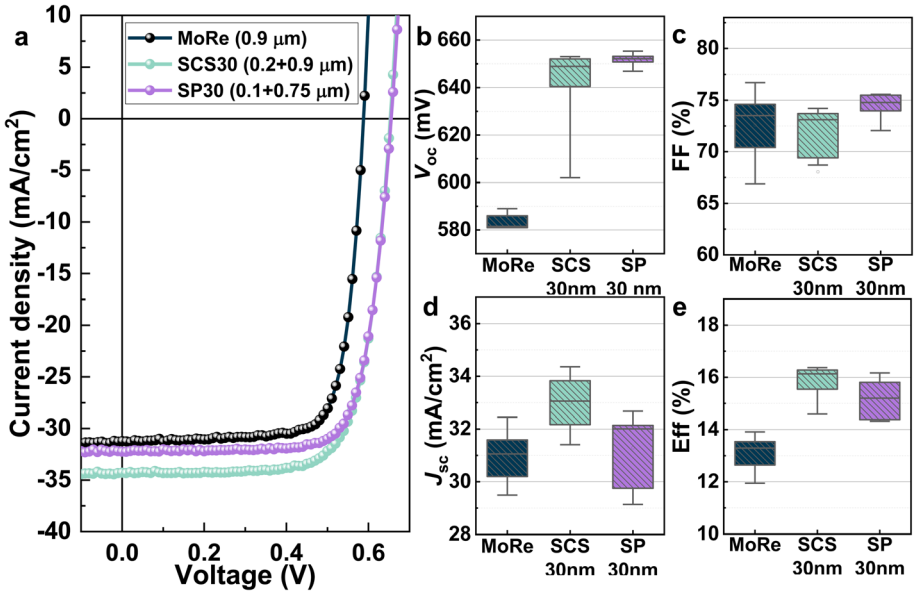

Fig. 5 (a) J–V characteristics under illumination of the reference solar cell and solar cells passivated by the Cu-annealed HTL with solution or sputter prepared 30 nm In_2O_3. Cu annealing is effective to improve hole transport properties of the HTL, leading to a higher FF. Here we show the best solar cells from each experiment. The statistical results of solar cell parameters: (b) open circuit voltage; (c) fill factor; (d) short circuit current and (e) active area efficiency.

while maintaining adequate passivation, thereby paving the way for highly efficient homogeneous CIGS solar cells with reduced thickness.

Varying thicknesses of In_2O_3 all lead to solar cells with a notable and comparable improvement in V_{oc}, as depicted in Fig. 4c. The majority of these solar cells demonstrate robust FFs ranging from 70% to 76%, as illustrated in Fig. S4 and S5. This indicates that Cu annealing is an effective way to make the GaO_x layer in the HTL conductive for holes. However, further investigation into the impact of annealing conditions—such as Cu quantity, vacuum level, annealing duration, and substrate temperature—on HTL properties may further improve the solar cells.

Efficiency improvement introduced by adding RbF PDT and heat light soaking

The Cu-annealed HTL demonstrates effective passivation and hole transport properties, thereby shifting the dominant

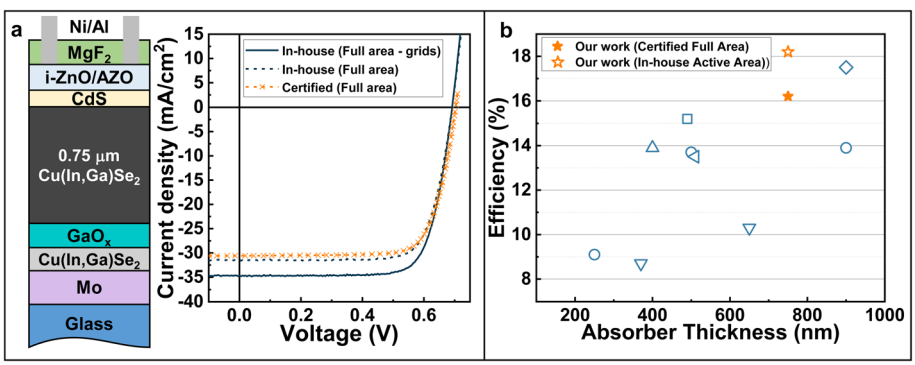

Sample		Area* cm²	CIGS thickness (μm)	V_{oc} mV	J_{sc} mA/cm²	FF %	Eff %
CIGSe+ARC	In house	0.219*	0.1+0.75	691.9	34.60	76.1	18.22
		0.241#		691.9	31.46	76.1	16.56
	Certified	0.241#		703.2(±2.3)	30.62(±0.42)	75.36(±0.46)	16.21(±0.25)

*: Active area = (Full area – grids); #: Full area

Fig. 6 (a) The device structure plus the in-house and certified J–V characteristics of the record sub-micron solar cell. (b) The efficiency of this record sub-micron CIGS cell compared to the efficiency of the best literature reported sub-micron CIGS solar cells. Circle,[69] square,[15] down triangle,[70] up triangle,[48] left triangle,[20] and diamond.[19]

efficiency limitation from backside recombination to bulk recombination, as previously discussed.[30] To enhance solar cell efficiency further, we have introduced RbF PDT and heat light soaking (HLS).[32,38,66,67] Initial outcomes reveal promising enhancements in ΔE_F. As depicted in Fig. 4a, by adding RbF PDT and heat light soaking, we achieved a Y_{PL} of 0.15% with a corresponding non-radiative ΔE_F deficit of approximately 165 meV, which is notably 60 meV lower than that of samples without RbF PDT and heat light soaking, suggesting a pathway to improve solar cell performance. However, the resultant solar cells exhibit S-shaped *J–V* curves with a reduced FF, V_{oc} and J_{sc}, as outlined in Fig. S6. This phenomenon may stem from excessive $RbInSe_2$ thickness due to an unoptimized RbF PDT, impeding electron transport.[68] Additionally, we cannot exclude the possibility that overdosing Rb and diffusion to the backside might change the HTL properties, consequently hindering hole transportation.

Further optimisation of the RbF yielded the best device in this study. As illustrated in Fig. 4a, our top-performing solar cell exhibits a suboptimal non-radiative ΔE_F loss of 205 meV, approximately 40 meV higher than the optimal case. However, the solar cell demonstrates a good FF of ~76% (Fig. 6a), resulting in an in-house measured (active area) efficiency of 18.2% with ARC. We had this cell certified at ISE CalLab and obtained a certified full-area efficiency of 16.2% (certified *J–V* curve is shown in Fig. S7). The difference is mainly due to our unoptimized grids which cause around 10% of shadowing loss to the J_{sc}. This efficiency ranks among the highest reported for sub-micron CIGS solar cells, as summarized in Fig. 6b. With further optimization, achieving efficiencies close to 20% for sub-micron CIGS (0.1 + 0.75 μm) and beyond 21% for slightly thicker CIGS (*e.g.*, 1.0 μm) seems very possible.

Conclusion

A novel HTL structure has been implemented in sub-micron CIGS solar cells, initially comprising CGS/In_2O_3 layers, which transforms into CIGS/GaO_x during absorber growth. This bilayer provides effective backside passivation without hampering hole transport. The backside passivation yields a notable increase in V_{oc} by 60–80 mV. In the absence of Cu annealing of the HTL, solar cells exhibit markedly low FFs, attributed to inadequate hole transport in the HTL. However, Cu annealing significantly enhances FFs to 77%, indicating a crucial enhancement in hole transport through the HTL. Moreover, the performance of sputtered In_2O_3 matches the one of solution prepared In_2O_3, facilitating potential large-scale manufacturing applications. With In_2O_3 thickness ranging from 20 to 40 nm, the passivation and hole transport of the Cu-annealed HTL are hardly impacted by In_2O_3 thickness variation. This flexibility eliminates the need for precise control within the range of a few nanometers, enhancing feasibility and adaptability for large-scale manufacturing. Furthermore, with additional RbF PDT and heat light soaking, we achieved a notable Y_{PL} of ~0.15% (non-radiative ΔE_F loss = ~165 meV) and established the best active area efficiency of 18.2% for sub-micron CIGS solar cells with an absorber thickness of 0.75 μm.

Methods

Sample preparation

Mo. 500 nm molybdenum is prepared by sputtering.

$CuGaSe_2$. 100–200 nm $CuGaSe_2$ is deposited by co-evaporation with a substrate setting temperature of 356 °C.

In_2O_3. In_2O_3 is prepared by solution combustion synthesis or sputtering.

Solution preparation. The precursor solution is formulated by dissolving 1203.2 mg of $In(NO_3)_3 \cdot xH_2O$ (99.99%, Sigma-Aldrich) in 20 mL of 2-methoxyethanol (2-MOE, 99.8%, Sigma-Aldrich), resulting in a 0.2 M concentration. Subsequently, 800 μL of acetylacetone ($C_5H_8O_2$, 99%, Sigma-Aldrich) is introduced as a fuel, followed by the addition of 360 μL of 14.5 M NH_3 (aqueous, 99%, Sigma-Aldrich) to adjust the pH and facilitate the formation of $In(acac)_x$ (acac = $C_5H_7O_2$) complexes of In ions. The solutions are then agitated until they achieve clarity. Using this clear solution, In_2O_3 films are produced by spin-coating onto substrates at 3000 rpm for 60 s, followed by hot-plate heating at 130 °C for 1 min. This spin-coating and drying process is repeated to attain film thicknesses of 20 nm, 30 nm, and 40 nm. Finally, the films are crystallized by placing the samples on a hot-plate in air at 300 °C for 3 min.

For sputtered passivated samples, the indium oxide (In_2O_3) layers are deposited using the RF sputtering technique. Various thicknesses of In_2O_3 are achieved by adjusting the deposition energies: 25 nm at 39 kJ, 30 nm at 46 kJ, 35 nm at 54 kJ, and 40 nm at 62 kJ.

Cu annealing of the HTL. Around 40 nm of Cu is deposited onto the surface of In_2O_3 at a substrate setting temperature of 200 °C. The temperature is then quickly increased to 500 °C at a rate of 50 °C per minute, after which a 20-minute annealing process is conducted under vacuum conditions of approximately 5×10^{-9} torr inside the MBE chamber that we use for absorber deposition. Next, the substrate temperature is gradually decreased to 356 °C at a rate of 20 °C per minute, after which the standard 3-stage process for CIGS preparation commences. For the high temperature process discussed below, the substrate temperature remains constant at 500 °C for the 1st stage, with no temperature reduction occurring.

Cu(In,Ga)Se_2. The absorber undergoes a standard 3-stage preparation process. For the best solar cell with an efficiency of 18.2%, initially, In–Ga–Se is supplied at a substrate temperature of 500 °C in the first stage. For the other samples, this temperature is 356 °C. Subsequently, during the second stage the substrate setting temperature is increased up to 580 °C at a rate of 20 °C per minute with co-evaporation of Cu and Se. Upon reaching a Cu-rich state (Cu/[In + Ga] ≈ 1.2, estimated based on the process times, *e.g.*, from the 1st stoichiometric point, the point where the output power of the substrate heater starts increasing), the Cu shutter closes, and the film undergoes a 5-minute annealing process in a Se atmosphere. In the third stage, maintaining the substrate temperature at 580 °C, In and Ga are reintroduced under Se pressure to achieve a final absorber state which is slightly Cu-deficient (Cu/[In + Ga] = 0.92–0.95, determined using EDS) with a thickness of

approximately 0.75 μm to 0.9 μm. Notably, the pyrometer readings for substrate temperature typically register lower values than the setting temperature. This discrepancy tends to increase with higher setting temperatures; for instance, at 365 °C, both readings are closer, while at 580 °C, the pyrometer indicates a temperature 50–60 °C lower than the setting temperature. During the absorber growth processes, the Se flux is around 4.5×10^{-6} torr which is determined by an ion gauge facing the Se source before and after the absorber growth.

RbF PDT. The RbF PDT is conducted after absorber deposition without interrupting the vacuum. Following the absorber deposition, the substrate setting temperature is lowered to 280 °C. From the pyrometer, the reading temperature is around 313 ± 5 °C. A subsequent 10-minute RbF PDT is performed by supplying RbF for 10 minutes under a Se atmosphere. The Se flux is around 2.5×10^{-6} torr, and the RbF source temperature is 450 °C.

CdS. The CdS layer is fabricated using chemical bath deposition. Prior to the CdS application, all samples undergo a 30-second chemical etching process using a 5% aqueous KCN solution, aimed at eliminating potential residual oxides. For the samples with RbF PDT, they are additionally etched by using 1.5 M NH_4OH for 3 minutes after KCN etching. The chemical bath process involves deposition for 6–7 minutes at 67 °C, utilizing a solution composed of 2 mM $CdSO_4$, 50 mM thiourea, and 1.5 M NH_4OH. Based on standard growth rates, the estimated thickness of the CdS layer ranges between 40 and 50 nm. This CdS layer plays a crucial role in passivating the front surface, effectively preventing surface degradation.

TCO and grids. To complete the device assembly, the i-ZnO/ZnO:Al layers are sequentially RF-sputtered atop the CdS layer, followed by the deposition of Ni/Al grids *via* e-beam evaporation. The transparent conducting oxide (TCO) deposition process was conducted using a commercial semi-automated sputtering deposition system. Two magnetron guns, outfitted with ceramic 3-inch diameter by 0.125-inch thick ZnO and ZnO:Al (2 wt% Al) targets, were powered by RF generators and operated within a non-reactive Ar atmosphere. The deposition of the non-conductive ZnO (i-ZnO) and conductive ZnO:Al (AZO) films involved applying sputtering powers of 125 and 140 W to the respective targets, while maintaining a pressure of 1 mTorr. The resulting thicknesses of the i-ZnO and AZO films are around 80 and 380 nm, respectively. Ni–Al grids are deposited by e-beam evaporation.

MgF anti-reflection coating (ARC). A 90 nm MgF ARC layer is evaporated by using an e-beam evaporator onto the top of the TCO layer and the grids to reduce the reflection losses.

Heat-light-soaking. The heat light soaking is done with a substrate setting temperature of 80 °C in a N_2 atmosphere and under an equivalent illumination intensity of 0.5 Sun for 3 hours. The samples are sealed in a transparent plastic bag that is purified and refilled with 99% pure dry N_2. Then samples are placed on a hot plate with a setting temperature of 80 °C under a LED light source (EACLL GU10-1050 Lumen and 6000 K bulbs) with an equivalent illumination intensity of 0.5 Sun, which means that the photon flux with energy above 1.12 eV is roughly half of that given by the AM1.5G spectrum.

Characterization

Time-resolved photoluminescence (TRPL). This technology relies on time-correlated single photon counting (TCSPC) to analyze luminescence decays in the time domain. Measurements are conducted using a 640 nm pulsed diode laser. For samples exhibiting short or long lifetimes, the laser repetition rate is set to 5 or 1 MHz respectively. The typical average power of the laser at a repetition rate of 2 MHz is 0.25 mW, with a laser diameter of approximately 0.8 mm. To mitigate the pile-up effect and prevent loss of long-lifetime photons, the ratio between the total count rate and repetition rate is maintained below 2% by adjusting the neutral density (ND) filters to modulate laser intensity if necessary. A 2-exponential decay function is employed to fit the PL decay curve:

$$I = I_0 + A_1 \exp\left(\frac{-t}{\tau_1}\right) + A_2 \exp\left(\frac{-t}{\tau_2}\right) \quad (1)$$

in which I represents the intensity of the PL counts, while I_0 is the fitted background counts. The parameters τ_1 and τ_2 correspond to the fitted lifetimes for the fast and slow decays, respectively. In our investigation, we specifically focus on τ_2, which is significantly impacted by backside recombination.[41]

Absolute PL. The absolute PL is measured using a home-built setup. All samples are excited by a diode laser with a wavelength of 660 nm and evaluated in ambient air at room temperature. The laser has an approximate diameter of 2.6 mm. Initial collection of photoluminescence involves two parabolic mirrors, redirecting the light to a monochromator *via* a 550 μm optical fiber. An InGaAs array detector captures the emitted light. The obtained PL spectra undergo spectral correction through calibration by using a halogen lamp with a known spectrum. Quantification of both excitation and corrected radiation flux is achieved using a power meter, enabling calculations of ΔE_F across specific illumination intensities ranging from 0.01 sun, or even lower, up to several sun equivalents, contingent upon the absorbers' quality and E_g. Here, one Sun intensity signifies that the photon flux matches the AM1.5 spectrum above the absorber's bandgap E_g. Applying Planck's generalized law:[71]

$$\phi_{PL}(E) \approx A(E)\phi_{bb}(E)\exp\left(\frac{\Delta E_F}{k_b T}\right) \quad (2)$$

in which $\phi_{PL}(E)$ is the measured PL spectrum, $\phi_{bb}(E)$ is the black body radiation, $A(E)$ is the absorptance and k_bT is the thermal energy. With the temperature fixed at the independently measured 295 K,[26,43] ΔE_F is computed by fitting the high-energy path of the PL spectra, assuming absorptance ($A(E)$) equals 1 in this energy range. However, it is important to note that this assumption leads to a slight underestimation of ΔE_F. Recent discussions have highlighted the impact of $A(E) < 1$ for high-energy photons.[26] With fitted ΔE_F, the $A(E)$ of the sample can be re-calculated from eqn (2). However, the 1st and 2nd diodes in our InGaAs array detector have different dark counts, which leads to non-smooth curves in a jagged shape. This issue becomes more serious when the PL signal is low. To have a smoother $A(E)$, thus having a better $dA(E)/dE$, the $A(E)$ shown

in Fig. 4b only contains the data that are collected from the second diode. This means that we have removed half of the pixels to minimize the influence of high dark counts on a low PL signal.

$$A(E) = \frac{\phi_{PL}(E)}{\phi_{bb}(E)} \exp\left(-\frac{\Delta E_F}{k_b T}\right) \quad (3)$$

The PL quantum yield (Y_{PL}) is determined by using the ratio between the absolute incident photon flux and PL flux. This approach also neglects reflection of laser photons and slightly underestimates Y_{PL}. The incident photon flux is determined by first measuring the actual power of the laser spot using a power meter. Subsequently, considering that the photon intensity conforms to a Gaussian distribution within its diameter, which is determined by using a CCD camera, the PL flux is then derived by integrating the absolute PL spectra across its emitted photon energy range. On knowing Y_{PL}, the non-radiative loss in ΔE_F ($\Delta\Delta E_F$) can be determined by:[26,42,43]

$$\Delta\Delta E_F = k_b T \times \ln(Y_{PL}) \quad (4)$$

Illumination current density–voltage (*J–V*). The measurements are conducted at 25 °C using a 4-probe configuration. A class AAA solar simulator provided a simulated AM1.5 G spectrum, calibrated using a Si reference cell. During the assessment, a forward scanning voltage ranging from −0.3 to 0.8 V is applied incrementally at intervals of 0.01 V with a waiting time of 0.25 s and scanning speed of 1 V s^{-1}. The certification measurements are done by Fraunhofer ISE CalLab PV Cells and certification can be found in Fig. S7.

External quantum efficiency (EQE). The EQE spectra are acquired using a home-built setup featuring a grating monochromator configuration under chopped illumination from halogen and xenon lamps. A lock-in amplifier facilitated the measurement of the solar cell's photocurrent. Calibration reference spectra are obtained using a calibrated Si detector covering the range of 300 to 1100 nm and a calibrated InGaAs detector spanning 1100 to 1400 nm. The measured solar cells are connected using 4 pins and measured in a 2-probe configuration.

Scanning electron microscopy (SEM). Scanning electron microscopy is used to analyze the cross-sectional microstructures of the films.

Transmission electron microscopy (TEM). In this study, cross-section Transmission Electron Microscopy (TEM) samples are meticulously prepared using a Focused Ion Beam (FIB) system, specifically the FEI Helios Nanolab 650. The TEM analysis is conducted using a JEOL F200-Cold FEG instrument. Elemental mapping and profiling are accomplished *via* X-ray Energy Dispersive Spectroscopy (EDS) in Scanning Transmission Electron Microscopy (STEM) mode.

Secondary ion mass spectrometry (SIMS). Measurements are conducted using a CAMECA SC-ultra instrument (Ametek). A 1 keV focused Cs^+ ion beam (16 nA) is utilized to sputter across a sample surface area measuring 500 μm × 500 μm. Only positive ions originating from the central region, with a diameter of 30 μm, are detected as MCs^+ or MCs_2^+, where M represents the ions of interest, such as Cu, In, Ga, Se, O, and Mo. Data are plotted against sputtering time that is related to depth in the stack.

Author contributions

T. W. conceived the idea and designed the experiments. L. S. prepared the oxides by solution combustion synthesis and wrote the part of paper about oxide preparation. T. W. wrote the rest of the paper. S. B. prepared the sputtered InO_x layers. T. W. and S. B. prepared the $Cu(In,Ga)Se_2$ absorbers. T. W. measured the PL of the samples and conducted the *J–V* and EQE measurements. M. M. made the most parts of the devices including glass cleaning and preparation of Mo, CdS, TCO and grids. M. M. also conducted the SEM measurements. N. V. and A. P. conducted the TEM and SIMS measurements and contributed to results discussion and analysis, A. P. also wrote the part about the TEM measurements. E. D., S. G., and S. S. were involved in results discussion and analysis and contributed to the improvement of experiments. S. S. defined the project, supervised this work and contributed to the writing of the paper. All the authors contributed to the revision of the paper.

Conflicts of interest

The authors declare that they have competing interests related to the patent associated with this work. The patent in question is WO2025/012117 A1 (International Publication No.) titled "Thin film solar cell and corresponding production method". The inventor Taowen Wang is an employee of the University of Luxembourg. The inventor Longfei Song is an employee of the Luxembourg Institute of Science and Technology (LIST). Both the University of Luxembourg and LIST hold the patent.

Data availability

Data for this article are available at Zenodo at **https://doi.org/10.5281/zenodo.15039028**.

Supplementary information: SEM cross-section image of a CIGS solar cell with HTL layer, the influence of GaO_x thickness on solar cell performance and certification of the record solar cell. See DOI: **https://doi.org/10.1039/d5el00049a**.

Acknowledgements

This work was supported by the Luxembourg National Research Fund (FNR) through the PACE project under the grant number of PRIDE17/12246511/PACE and by the European Union in the framework of the HiBITS project. The authors thank Brahime El Adib for his technical assistance in SIMS characterization. ChatGPT, a language model developed by OpenAI in San Francisco, CA, USA, provided assistance in English language editing. The whole text has been carefully modified and verified by the authors. For the purpose of open access, the author has applied

References

1 J. Keller, K. Kiselman, O. Donzel-Gargand, N. M. Martin, M. Babucci, O. Lundberg, E. Wallin, L. Stolt and M. Edoff, *Nat. Energy*, 2024, **9**, 467–478.
2 M. Powalla, S. Paetel, D. Hariskos, R. Wuerz, F. Kessler, P. Lechner, W. Wischmann and T. M. Friedlmeier, *Engineering*, 2017, **3**, 445–451.
3 B. H. King, J. S. Stein, D. Riley, C. B. Jones and C. D. Robinson, in *Degradation assessment of fielded CIGS photovoltaic arrays: Proceedings of the in 2017 IEEE 44th Photovoltaic Specialist Conference (PVSC)*, Washington, 2017.
4 S. Siebentritt and T. Weiss, *Sci. China:Phys., Mech. Astron.*, 2023, **66**, 217301.
5 N. Dahan, Z. Jehl, T. Hildebrandt, J.-J. Greffet, J.-F. Guillemoles, D. Lincot and N. Naghavi, *J. Appl. Phys.*, 2012, **112**(9), 530–544.
6 C. Colin, I. Massiot, A. Cattoni, N. Vandamme, C. Dupuis, N. Bardou, I. Gerard, J.-F. Guillemoles and J.-L. Pelouard, *Proc. SPIE 8620, Physics, Simulation, and Photonic Engineering of Photovoltaic Devices II*, 2013, vol. 86200C.
7 E. Jarzembowski, B. Fuhrmann, H. Leipner, W. Fränzel and R. Scheer, *Thin Solid Films*, 2017, **633**, 61–65.
8 F. Mollica, M. Jubault, F. Donsanti, A. Loubat, M. Bouttemy, A. Etcheberry and N. Naghavi, *Thin Solid Films*, 2017, **633**, 202–207.
9 T. Schneider, J. Tröndle, B. Fuhrmann, F. Syrowatka, A. Sprafke and R. Scheer, *Sol. RRL*, 2020, **4**, 2000295.
10 W. Sharaman, R. Birkmire, S. Marsillac, M. Marudachalam, N. Orbey and T. Russell, *Conference Record of the Twenty Sixth IEEE Photovoltaic Specialists Conference*, 1997.
11 M. Gloeckler and J. R. Sites, *J. Appl. Phys.*, 2005, **98**, 103703.
12 E. Jarzembowski, F. Syrowatka, K. Kaufmann, W. Fränzel, T. Hölscher and R. Scheer, *Appl. Phys. Lett.*, 2015, **107**, 051601.
13 T. P. Weiss, B. Bissig, T. Feurer, R. Carron, S. Buecheler and A. N. Tiwari, *Sci. Rep.*, 2019, **9**, 1–13.
14 J. Kavalakkatt, D. Abou-Ras, J. Haarstrich, C. Ronning, M. Nichterwitz, R. Caballero, T. Rissom, T. Unold, R. Scheer and H. W. Schock, *J. Appl. Phys.*, 2014, **115**, 014504.
15 L. M. Mansfield, A. Kanevce, S. P. Harvey, K. Bowers, C. Beall, S. Glynn and I. L. Repins, *Prog. Photovoltaics Res. Appl.*, 2018, **26**, 949–954.
16 T. Wang, F. Ehre, T. P. Weiss, B. Veith-Wolf, V. Titova, N. Valle, M. Melchiorre, O. Ramírez, J. Schmidt and S. Siebentritt, *Adv. Energy Mater.*, 2022, 2202076.
17 K. Ramanathan, R. Noufi, B. To, D. Young, R. Bhattacharya, M. Contreras, R. Dhere and G. Teeter, *Processing and Properties of Sub-Micron CIGS Solar Cells*, Photovoltaic Energy Conversion Conference Record of the IEEE, 2006, vol. 1, pp. 380–383.
18 Y. Kong, J. Li, Z. Ma, Z. Chi and X. Xiao, *J. Mater. Chem. A*, 2020, **8**, 9760–9767.
19 S. Yang, J. Zhu, X. Zhang, X. Ma, H. Luo, L. Yin and X. Xiao, *Prog. Photovoltaics Res. Appl.*, 2015, **23**, 1157–1163.
20 L. Gouillart, A. Cattoni, W. C. Chen, J. Goffard, L. Riekehr, J. Keller, M. Jubault, N. Naghavi, M. Edoff and S. Collin, *Prog. Photovoltaics Res. Appl.*, 2021, **29**, 212–221.
21 T. Dullweber, O. Lundberg, J. Malmström, M. Bodegård, L. Stolt, U. Rau, H.-W. Schock and J. H. Werner, *Thin Solid Films*, 2001, **387**, 11–13.
22 Y. H. Chang, R. Carron, M. Ochoa, C. Bozal-Ginesta, A. N. Tiwari, J. R. Durrant and L. Steier, *Adv. Energy Mater.*, 2021, **11**, 2003446.
23 C. Spindler, F. Babbe, M. H. Wolter, F. Ehré, K. Santhosh, P. Hilgert, F. Werner and S. Siebentritt, *Phys. Rev. Mater.*, 2019, **3**, 090302.
24 R. Carron, E. Avancini, T. Feurer, B. Bissig, P. A. Losio, R. Figi, C. Schreiner, M. Bürki, E. Bourgeois and Z. Remes, *Sci. Technol. Adv. Mater.*, 2018, **19**, 396–410.
25 U. Rau, B. Blank, T. C. Müller and T. Kirchartz, *Phys. Rev. Appl.*, 2017, **7**, 044016.
26 S. Siebentritt, U. Rau, S. Gharabeiki, T. P. Weiss, A. Prot, T. Wang, D. Adeleye, M. Drahem and A. Singh, *Faraday Discuss.*, 2022, **239**, 112–129.
27 B. J. Stanbery, D. Abou-Ras, A. Yamada and L. Mansfield, *J. Phys. D: Appl. Phys.*, 2021, **55**, 173001.
28 E. Yablonovitch, T. Gmitter, R. Swanson and Y. Kwark, *Appl. Phys. Lett.*, 1985, **47**, 1211–1213.
29 U. Rau and T. Kirchartz, *Adv. Mater. Interfaces*, 2019, **6**, 1900252.
30 T. Wang, L. Song, S. Gharabeiki, M. Sood, J. C. Aubin, M. Prot, R. G. Poeira, M. Melchiorre, N. Valle, A. Marie Philippe, S. Glinsek, E. Defay, P. J. Dale and S. Siebentritt, *Sol. RRL*, 2024, **8**(12), 2400212.
31 A. M. Gabor, J. R. Tuttle, D. S. Albin, M. A. Contreras, R. Noufi and A. M. Hermann, *Appl. Phys. Lett.*, 1994, **65**, 198–200.
32 P. Jackson, R. Wuerz, D. Hariskos, E. Lotter, W. Witte and M. Powalla, *Phys. Status Solidi RRL*, 2016, **10**, 583–586.
33 T. Wada, N. Kohara, T. N. T. Negami and M. N. M. Nishitani, *Jpn. J. Appl. Phys.*, 1996, **35**, L1253.
34 D. Abou-Ras, G. Kostorz, D. Bremaud, M. Kälin, F. Kurdesau, A. Tiwari and M. Döbeli, *Thin Solid Films*, 2005, **480**, 433–438.
35 A. Chirilă, S. Buecheler, F. Pianezzi, P. Bloesch, C. Gretener, A. R. Uhl, C. Fella, L. Kranz, J. Perrenoud and S. Seyrling, *Nat. Mater.*, 2011, **10**, 857–861.
36 A. Niemegeers, M. Burgelman, R. Herberholz, U. Rau, D. Hariskos and H. W. Schock, *Prog. Photovoltaics Res. Appl.*, 1998, **6**, 407–421.
37 G. Sozzi, F. Troni and R. Menozzi, *Sol. Energy Mater. Sol. Cells*, 2014, **121**, 126–136.
38 T. Kodalle, M. D. Heinemann, D. Greiner, H. A. Yetkin, M. Klupsch, C. Li, P. A. van Aken, I. Lauermann, R. Schlatmann and C. A. Kaufmann, *Sol. RRL*, 2018, **2**, 1800156.
39 P. Jackson, D. Hariskos, R. Wuerz, O. Kiowski, A. Bauer, T. M. Friedlmeier and M. Powalla, *Phys. Status Solidi RRL*, 2015, **9**, 28–31.

40 M. Edoff, T. Jarmar, N. S. Nilsson, E. Wallin, D. Högström, O. Stolt, O. Lundberg, W. Shafarman and L. Stolt, *IEEE J. Photovoltaics*, 2017, **7**, 1789–1794.
41 J. Moseley, D. Krasikov, C. Lee and D. Kuciauskas, *J. Appl. Phys.*, 2021, **130**(16), 163105.
42 L. Krückemeier, U. Rau, M. Stolterfoht and T. Kirchartz, *Adv. Energy Mater.*, 2020, **10**, 1902573.
43 S. Siebentritt, T. P. Weiss, M. Sood, M. H. Wolter, A. Lomuscio and O. Ramirez, *J. Phys.: Mater.*, 2021, **4**, 042010.
44 M. Sood, A. Urbaniak, C. Kameni Boumenou, T. P. Weiss, H. Elanzeery, F. Babbe, F. Werner, M. Melchiorre and S. Siebentritt, *Prog. Photovoltaics Res. Appl.*, 2022, **30**, 263–275.
45 J. Zhang, S. Zhu, C. Gao, C. Gao and X. Liu, *Sol. RRL*, 2022, **6**, 2100861.
46 J. Zhang, S. Zhu, Q. Yang, C. Gao and X. Liu, *Sol. RRL*, 2023, 2300263.
47 D. Ledinek, O. Donzel-Gargand, M. Sköld, J. Keller and M. Edoff, *Sol. Energy Mater. Sol. Cells*, 2018, **187**, 160–169.
48 B. Vermang, J. T. Wätjen, V. Fjällström, F. Rostvall, M. Edoff, R. Kotipalli, F. Henry and D. Flandre, *Prog. Photovoltaics Res. Appl.*, 2014, **22**, 1023–1029.
49 Y. S. Lee, T. Gershon, T. K. Todorov, W. Wang, M. T. Winkler, M. Hopstaken, O. Gunawan and J. Kim, *Adv. Energy Mater.*, 2016, **6**, 1600198.
50 G. S. Park, S. Lee, D. S. Kim, S. Y. Park, J. H. Koh, D. H. Won, P. Lee, Y. R. Do and B. K. Min, *Adv. Energy Mater.*, 2023, **13**, 2203183.
51 F. Werner, B. Veith-Wolf, C. Spindler, M. R. Barget, F. Babbe, J. Guillot, J. Schmidt and S. Siebentritt, *Phys. Rev. Appl.*, 2020, **13**, 054004.
52 B. Vermang, J. T. Wätjen, V. Fjällström, F. Rostvall, M. Edoff, R. Gunnarsson, I. Pilch, U. Helmersson, R. Kotipalli and F. Henry, *Thin Solid Films*, 2015, **582**, 300–303.
53 B. Vermang, V. Fjällström, X. Gao and M. Edoff, *IEEE J. Photovoltaics*, 2013, **4**, 486–492.
54 G. Rajan, K. Aryal, S. Karki, P. Aryal, R. W. Collins and S. Marsillac, *J. Spectrosc.*, 2018, **2018**, 8527491.
55 U. Rau and J. Werner, *Appl. Phys. Lett.*, 2004, **84**, 3735–3737.
56 R. Carron, C. Andres, E. Avancini, T. Feurer, S. Nishiwaki, S. Pisoni, F. Fu, M. Lingg, Y. E. Romanyuk and S. Buecheler, *Thin Solid Films*, 2019, **669**, 482–486.
57 T. Kirchartz and U. Rau, *J. Appl. Phys.*, 2007, **102**(10), 104510.
58 S. Siebentritt, G. Rey, A. Finger, D. Regesch, J. Sendler, T. P. Weiss and T. Bertram, *Sol. Energy Mater. Sol. Cells*, 2016, **158**, 126–129.
59 M. H. Wolter, R. Carron, E. Avancini, B. Bissig, T. P. Weiss, S. Nishiwaki, T. Feurer, S. Buecheler, P. Jackson and W. Witte, *Prog. Photovoltaics*, 2022, **30**, 702–712.
60 I. Studenyak, M. Kranjčec and M. Kurik, *Int. J. Opt. Appl.*, 2014, **4**, 96–104.
61 J. H. Werner, J. Mattheis and U. Rau, *Thin Solid Films*, 2005, **480**, 399–409.
62 S. Siebentritt, *Sol. Energy Mater. Sol. Cells*, 2011, **95**, 1471–1476.
63 O. Ramírez, J. Nishinaga, F. Dingwell, T. Wang, A. Prot, M. H. Wolter, V. Ranjan and S. Siebentritt, *Sol. RRL*, 2023, **7**, 2300054.
64 A. M. Bothwell, J. Wands, M. F. Miller, A. Kanevce, S. Paetel, P. Tsoulka, T. Lepetit, N. Barreau, N. Valdes and W. Shafarman, *Sol. RRL*, 2023, **7**, 2300075.
65 M. H. Wolter, B. Bissig, E. Avancini, R. Carron, S. Buecheler, P. Jackson and S. Siebentritt, *IEEE J. Photovoltaics*, 2018, **8**, 1320–1325.
66 S. Siebentritt, E. Avancini, M. Bär, J. Bombsch, E. Bourgeois, S. Buecheler, R. Carron, C. Castro, S. Duguay and R. Félix, *Adv. Energy Mater.*, 2020, **10**, 1903752.
67 S. Ishizuka, N. Taguchi, J. Nishinaga, Y. Kamikawa, S. Tanaka and H. Shibata, *J. Phys. Chem. C*, 2018, **122**, 3809–3817.
68 T. P. Weiss, S. Nishiwaki, B. Bissig, R. Carron, E. Avancini, J. Löckinger, S. Buecheler and A. N. Tiwari, *Adv. Mater. Interfaces*, 2018, **5**, 1701007.
69 K. Kim, H. Park, W. K. Kim, G. M. Hanket and W. N. Shafarman, *IEEE J. Photovoltaics*, 2012, **3**, 446–450.
70 A. Duchatelet, E. Letty, S. Jaime-Ferrer, P.-P. Grand, F. Mollica and N. Naghavi, *Sol. Energy Mater. Sol. Cells*, 2017, **162**, 114–119.
71 P. Würfel, *Physics of Solar Cells*, Wiley-VCH Verlag GmbH, Weinheim, 2005.